Journal of Materials Science & Technology 142 (2023) 89–97

Contents lists available at ScienceDirect

Journal of Materials Science & Technology

journal homepage: www.elsevier.com/locate/jmst

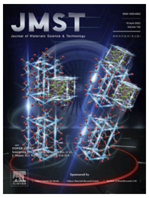

Research Article

Pressure-driven anomalous thermal transport behaviors in gallium arsenide

Zhongyin Zhang, Xuanhui Fan, Jie Zhu*, Kunpeng Yuan, Jing Zhou, Dawei Tang*

Key Laboratory of Ocean Energy Utilization and Energy Conservation of Ministry of Education, Dalian University of Technology, Dalian 116023, China

ARTICLE INFO

Article history:
Received 9 June 2022
Revised 13 October 2022
Accepted 29 October 2022
Available online 17 November 2022

Keywords:
Gallium arsenide
High pressure
Thermal conductivity
Interfacial thermal conductance
Time domain thermoreflectance

ABSTRACT

High-pressure has been widely utilized to improve material performances such as thermal conductivity κ and interfacial thermal conductance G. Gallium arsenide (GaAs) as a functional semiconductor has attracted extensive attention in high-pressure studies for its technological importance and complex structure transitions. Thermal properties of GaAs under high pressure are urgent needs in physics but remain elusive. Herein, we systematically investigate κ_{GaAs} and $G_{\mathrm{Al/GaAs}}$ of multi-structure up to ~23 GPa. We conclude that: (1) in pressurization, phonon group velocity, lattice defects, and electrons play a central role in κ_{GaAs} in elastic, plastic, and metallization regions, respectively. The increased phonon density of states (PDOS) overlap, group velocity, and interfacial bonding enhances $G_{\mathrm{Al/GaAs}}$. (2) In depressurization, electrons remain the dominant factor on κ_{GaAs} from 23 to 13.5 GPa. $G_{\mathrm{Al/GaAs}}$ increases dramatically at ~12 GPa due to the larger PDOS overlap. With decompressing to ambient, lattice defects including grain size reduction, arsenic vacancies, and partial amorphization reduce κ_{GaAs} to a glass-like value. Remarkably, the released $G_{\mathrm{Al/GaAs}}$ is 2.6 times higher than that of the initial. Thus our findings open a new dimension in synergistically realizing glass-like κ and enhancing G, which can facilitate thermoelectric performance and its potential engineering applications.

1. Introduction

Moving from condensed-matter to dense-matter physics, the extensive properties of materials change and unexpected physical phenomena occur. Utilizing high pressure, therefore, is an efficient and powerful method to modulate the structure and physical properties of materials in a wide range, such as the synthesis of new compounds [1], semiconductor-metal transitions [2,3], electron-phonon coupling factors [4], thermoelectric performances [5], and thermal properties [6]. Among them, applying high pressure to realize the modulation of thermal properties has received a great deal of attention for its important applications in energy conversions [5,7,8], geophysics [9], and high-temperature superconductors [10]. The knowledge of thermal transport behaviors in amorphous [11] and crystalline [12–14] materials under high-pressure assists in building a basis for extrapolation to more extreme pressure-temperature conditions.

Among III–V binary semiconductors, gallium arsenide (GaAs), widely used in optoelectronics and microelectronics [15,16], has attracted extensive attention in high-pressure studies. This interest has arisen owing to the technological importance of GaAs, coupled with the fact that GaAs exhibits a multiple and complex phase change under high pressure. In the pressurization process, early experimental work suggested that GaAs existed a high-pressure metallic phase namely an orthorhombic distortion of β-Sn [17], however, *ab initio* calculations supported the views that the first-order phase transition from zinc blende (*ZB*) should be to a distorted tetrahedral structure SC16 [18]. More accurate x-ray diffraction experiments identified the β-Sn was in fact a *Cmcm* structure that appeared at 15–17 GPa [19]. Regarding to the depressurization process, several experimental [20] and theoretical [21] studies have proved that a Cinnabar phase appeared at ~12 GPa on pressure decrease from the *Cmcm* structure. With the *Cmcm*-GaAs heated to above ~400 K at ~14 GPa, the SC16 phase was observed and was found to be stable at room temperature [22]. More recently, a Wurtzite phase was first identified existing in GaAs after pressure decreased from high-pressure SC16 phase to the ambient [23]. Besson and his colleagues [24] have also investigated the high-pressure phase transition and diagram of GaAs, finding that its structure is not reversible in the cycle of compression and decompression, accompanied by lattice defects, variation in atomic coordination number, and local amorphization. Therefore, high-pressure behaviors of GaAs are complex and are of great impor-

---

* Corresponding authors.
E-mail addresses: zhujie@dlut.edu.cn (J. Zhu), dwtang@dlut.edu.cn (D. Tang).

https://doi.org/10.1016/j.jmst.2022.10.009
1005-0302/

tance for crystalline phase engineering. Its performance changes, such as thermal transport, corresponding to the complex structural transitions is an interesting and challenging issue.

Prior experimental and theoretical studies demonstrated that pressure can increase phonon group velocity and simultaneously reduce the relaxation time. And it can also introduce lattice defects and induce semiconductor-metal transitions. Therefore, the pressure-dependent thermal measurement of GaAs offers an opportunity to experimentally explore the relationship between heat carriers (phonons, defects, and electrons) and thermal transport behaviors. Nevertheless, it has been pointed out that pressure-dependent thermal properties are urgent needs in physics but remain a significant challenge due to the difficulty in measurements [25].

Recently, some efforts have been made to investigate the pressure effect on the thermal conductivity (κ) and interfacial thermal conductance (G) of materials. The first-principles calculations have been used to study the κ of crystals under high pressure and temperature such as MgO [9,12], BaP [26], and GaAs [27]. Nevertheless, the calculation results are inconsistent and need to be further identified by proper experiments. Hsieh and his co-workers [11,28] made a great contribution to the measurement of κ at high pressure. They combined the time domain thermoreflectance (TDTR) technique with a diamond anvil cell (DAC) and measured the κ of amorphous polymers [11] up to 12 GPa and layered muscovite crystals [28] up to 24 GPa. Subsequently, TDTR integrated with the DAC was also employed to investigate semiconductor-metal phase transitions in bulk Si and $Si_{0.991}Ge_{0.009}$ [13] and MoS_2 [14]. Moreover, utilizing pressure to tune G of metal/dielectric has also attracted much attention. Generally, the interface acts as a low-pass filter, reflecting high-frequency modes while transmitting those low-frequency modes. However, at the pressure in the tens of GPa, comparable to the bulk modulus of many materials, the phonon density of states (PDOS) of both sides of materials extends to significantly higher frequencies, making interfacial thermal transport more complex. It has been proved that pressure can enhance the G of weak interfaces to a high-value characteristic by increasing the stiffness of interfacial bonds [29–31]. Therefore, it is important to explore the thermal transport of materials under high pressure, and TDTR integrated with the DAC is the most proper method.

Nevertheless, experimental investigations on pressure-dependent thermal properties of GaAs, especially the contribution of phonons, defects, and electrons at different high-pressure structures, have never been reported. Herein, we conducted systematically experimental studies on the κ_{GaAs} and $G_{Al/GaAs}$ during pressurization and depressurization processes. Firstly, the GaAs samples for TDTR and high-pressure Raman tests were prepared and loaded into the DAC. Then, TDTR integrated with the DAC was employed to characterize the pressure-dependent κ_{GaAs} and $G_{Al/GaAs}$. High-pressure Raman spectroscopy was also applied to study structure transitions in GaAs. Finally, combined with first-principles calculations and molecular dynamics (MD) simulation, the competing relationship of phonons, defects, and electrons in different pressure zones, which made the κ_{GaAs} and $G_{Al/GaAs}$ exhibit an anomalous pressure-dependent behavior, was fully discussed.

2. Experiment details

2.1. Sample preparations

The single crystal GaAs were supplied by Hefei kejing materials technology co., Ltd. To ensure the samples loaded into the DAC smoothly, we thinned it to ~20 μm in thickness. For a standard TDTR experiment, the thinned GaAs was coated with a layer of aluminum (Al) film by dc magnetron sputtering and the ambient thickness of the Al film was *in-situ* measured by picosecond acoustics [32] as ~ 96 nm. The Al film thermal conductivity was approximately 130 W m^{-1} K^{-1}, which was determined by a four-probe method and the Wiedemann-Franz law. Briefly, in the high-pressure experiment, a symmetrical DAC with a 300 μm culet size was used to generate high pressure. A stainless-steel gasket was pre-indented to ~50 μm in thickness and then was drilled a circle hole of 150 μm in diameter as a sample chamber. Subsequently, the GaAs, silicone oil, and ruby balls were loaded into the sample chamber. The silicone oil acted as the pressure-transmitting medium for improving the hydrostatic condition and the ruby balls were pressure calibrators [33]. The schematic diagram of the DAC and sample as well as the optical micrograph of the sample chamber are shown in Fig. 1(a–c), respectively. The ruby spectra at the selected pressure of pressurization (pink lines) and depressurization (blue lines) were shown in Fig. 1(d). The standard deviation of measured pressure is within 1 GPa.

2.2. Time domain thermoreflectance measurements

TDTR, a powerful and noncontact technique, was employed to investigate the thermal properties of GaAs during both pressurization and depressurization processes. The experimental details of TDTR have been explained thoroughly elsewhere [34–36]. but, briefly, a mode-locked Ti:sapphire laser with 785 nm in wavelength, 280 fs in pulse width, and 80 MHz in repetition rates, is split into a pump beam and a probe beam. The pump beam is modulated at 9.8 MHz and creates a temperature rise at the surface of the metal film. The probe beam, which is mechanically chopped at 200 Hz to remove background noise [37], subsequently monitors the change in reflectivity induced by temperature evolution. A mechanical delay stage advances the arrival time of the pump beam relative to the probe beam. The reflected probe beam is collected by a photodiode detector and the small voltage is picked up by a lock-in amplifier. The ratio of in-phase (V_{in}) signals and out-of-phase (V_{out}) signals is compared with a bidirectional heat transport model [38] to obtain unknown thermal properties, such as κ and G. The incident power is 20 mW for the pump beam and 10 mW for the probe beam, respectively, and the two beams have almost equal spot size, which is ~12 μm of $1/e^2$ radius.

2.3. High-pressure Raman spectroscopy

In this work, high-pressure Raman scattering was employed to investigate the structure and phonon behaviors of GaAs up to ~23 GPa. Raman scattering was performed at room temperature using a laser confocal Raman spectroscopy (LabRAM HR Evolution), with a 532 nm excitation line and an 1800 grooves mm^{-1} grating. For the excitation, the laser power was 100 mW and the spot size was ~5 μm. All spectra were collected with a backscattering geometry by an achromatic doublet lens and a CCD cooled by liquid nitrogen. The accumulated time was 50 ms and we repeated three times to remove fake peaks.

2.4. Phonon density of states calculations

To elucidate the underlying mechanism of thermal transport across interfaces between Al and GaAs, we calculate the PDOS. The first-principles density functional theory is employed to calculate the PDOS of crystalline Al and GaAs. For the accurate prediction of the PDOS, we need the input of second-order interatomic force constants, which are calculated by density functional perturbation theory on 4 × 4 × 4 q-mesh. All first-principles calculations are performed using the plane-wave-based QUANTUM ESPRESSO

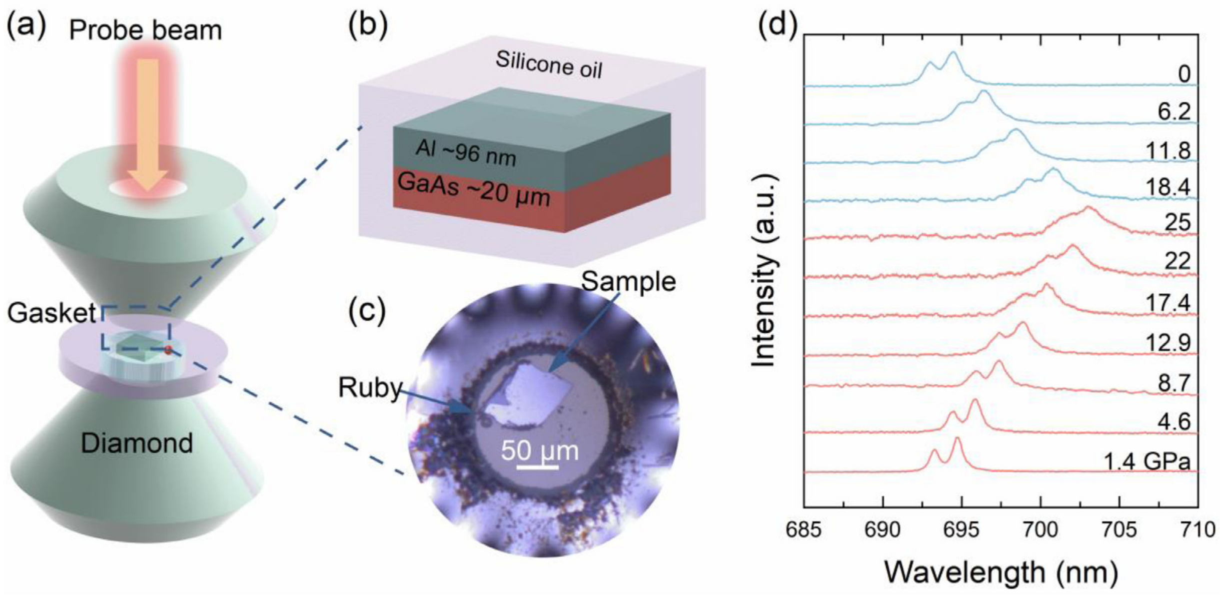

Fig. 1. Structure schematic diagrams of the DAC (a) and the sample (b). (c) The micrograph of the sample chamber. Ruby balls and the sample are labeled with arrows. (d) The selected ruby spectra of pressurization (pink lines) and depressurization (light blue lines).

package [39] based on the norm-conserving pseudopotentials constructed by the Perdew-Burke-Ernzerhof (PBE) generalized gradient density functional [40]. The kinetic-energy cut-off of the plane-wave basis is set to be 80 Ry. A well-converged 12 × 12 × 12 k-mesh is adopted to sample the first Brillouin zone. Both lattice constants and atomic coordinates are fully relaxed at each pressure, and the pressure is exerted uniformly in all directions. The convergence tolerance for the atomic force and the pressure are 10–6 Ry/Bohr and 0.5 kbar, respectively.

For amorphous GaAs, we resort to classical molecular dynamics with the LAMMPS package [41]. An analytic bond-order potential [42] is used to describe the interactions of the GaAs system. The model system is constructed from an 8 × 8 × 8-unit cell of GaAs, which consists of 4096 atoms. To generate the amorphous structure, the entire system is firstly heated from 300 to 3000 K in 300 ps with NPT ensemble and time interval of 0.5 fs. After that, the system is equilibrated at 3000 K for 100 ps. Then, we slowly quench the structure to 300 K at a rate of 1012 K s^{-1}. The system is further relaxed at 300 K for 100 ps. Finally, the fully relaxed structure is switched to the NVE ensemble for 100 ps and the atomic velocities are outputted every 10 steps. The PDOS of amorphous GaAs is calculated by taking the Fourier transform of the atomic velocity autocorrelation function. Besides, the PDOS overlap factor is defined as the integral of the overlap regions over the integral of the PDOS of Al.

3. Results and discussion

3.1. Structural transitions and vibrational properties of GaAs under high-pressure

High-pressure Raman spectroscopy enables us to reveal the mechanism of pressure effect on structural transitions and vibrational properties of GaAs. Selection rules in Raman spectroscopy, which predict certain vibrational modes to have zero intensities, give evidence of the symmetry or asymmetry of crystals. The shift of the characteristic frequency contains microcrystal size information [24].

As shown in Fig. 2(a), with the increase of pressure, the two characteristic modes (TO and LO) shift to the high wavenumber. When pressure is above ~16 GPa, they are gradually forbidden, demonstrating that the *ZB*-GaAs (semiconductor) transforms to the *Cmcm*-GaAs (metal). The critical point of phase transition obtained in this work matches well with the literature [20]. It should be noted here that the *ZB*-GaAs not completely transforms into *Cmcm*-GaAs, namely the two-phase coexistence, which can be proved by the sample's optical micrographs and the Raman scattering results. As shown in Fig. 2(b), the morphology of GaAs appears obvious metallic-luster when pressure is above ~16 GPa and the proportion of metallic phases increases monotonously with pressure. The Raman analysis on "dark" (*ZB*-GaAs) and "light" (*Cmcm*-GaAs) regions at ~17 GPa shown in Fig. 2(c) also gives direct evidence that GaAs exhibits a mixed phase in the range of 16–24 GPa. Besides, we also notice that the intensities of TO and LO modes have a resonant value at ~9 GPa (Fig. 2(d)), which implies that the energy of incident light (2.33 eV) almost equals to the band gap of GaAs so that strong interband transitions occur. A noteworthy feature is that the ratio of LO to TO intensities is asymmetrical with respect to the resonance, which means that the crystal is perturbed through local structural defects and crystallites' disorientation [24]. The Grüneisen parameter $\gamma = \frac{K}{\omega}\frac{\mathrm{d}\omega}{\mathrm{d}p}$, a direct assessment of the anharmonicity of the bonds, is likewise calculated for TO and LO lines. As shown in Fig. 2(e), the γ has a negative correlation with pressure, indicating that pressure benefits the harmonicity of optical phonons [43].

The structural and vibrational information of GaAs during the depressurization process is also investigated. Fig. 3(a) shows the Raman spectra of decompression. We find that the TO and LO modes do not reappear until at ~6.4 GPa. This consists of the observation from the micrographs shown in Fig. 3(b). It suggests that while the GaAs is released from higher pressure, spectral characteristics of Raman spectroscopy exhibit a relaxation feature called hysteresis, which is in agreement with the literature [44]. In Fig. 3(c), the pressure dependence of the two modes can be fitted as $\omega_{\mathrm{TO}} = 267.51 + 4.28p - 0.026p^2$ and $\omega_{\mathrm{LO}} = 289.84 + 4.53p - 0.064p^2$, where ω is in cm^{-1} and p in GPa. Both TO and LO modes of released GaAs shift towards lower frequency. Besides, we also note that there are two new features named A and B in Fig. 3(a). Furthermore, we compare the Raman spectra of the initial sample with the released sample in Fig. 3(d). Although the

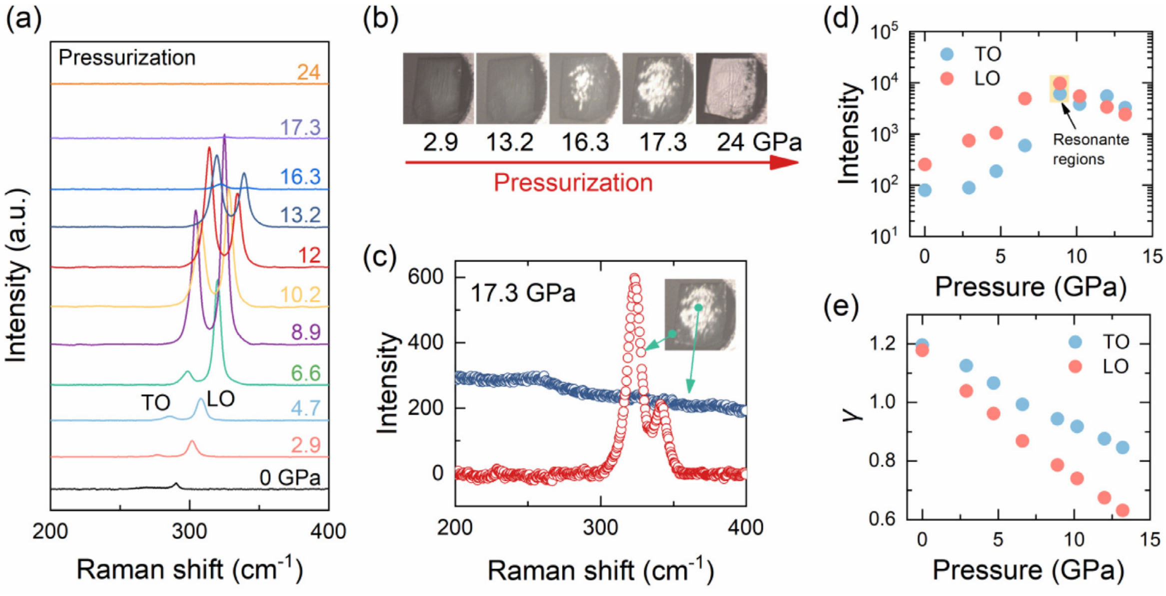

Fig. 2. Raman analysis of GaAs in the pressurization process. (a) The Raman spectra of GaAs in the pressurization process. TO is transverse optical phonons and LO is longitudinal optical phonons. (b) The morphology evolution of GaAs. (c) The Raman spectra of “light” and “dark” regions in GaAs under 17.3 GPa. The measurement area is labeled with blue circles. (d) The intensities of TO and LO modes as functions of pressure. (e) The Grüneisen parameter of TO and LO modes as functions of pressure.

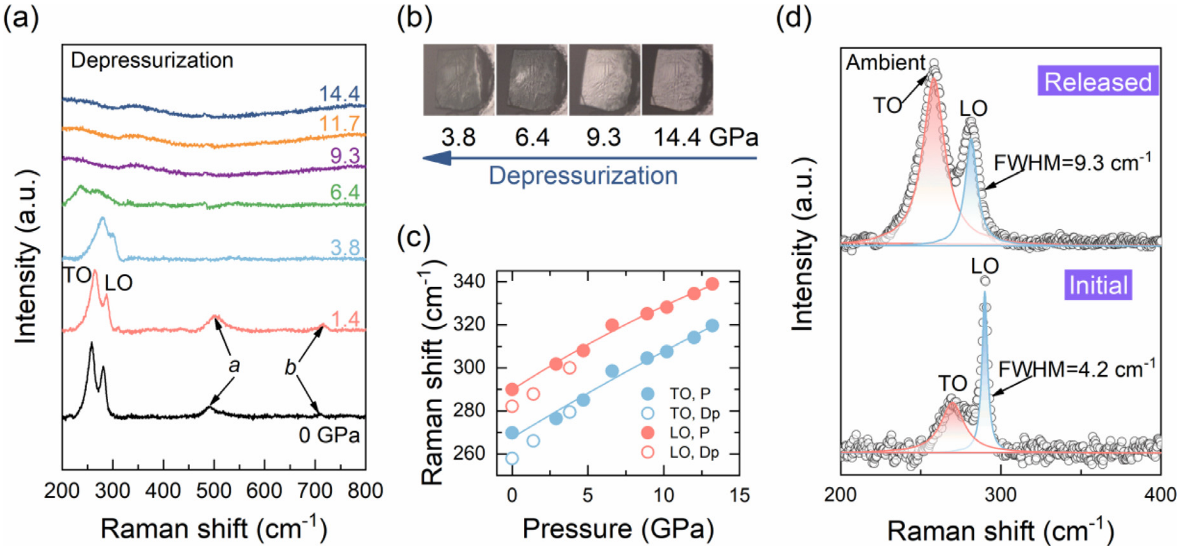

Fig. 3. Raman analysis of GaAs in the depressurization process. (a) The Raman spectra of GaAs in the depressurization process. A and B represent two new features, which indicate that the selection rules are perturbed. (b) The morphology evolution of GaAs during depressurization. (c) The pressure-dependence of TO and LO frequencies. Filled circles represent pressurization and open circles represent depressurization. (d) The Raman spectra of the initial GaAs and released GaAs at ambient conditions.

released GaAs has clear lattice vibration peaks, the intensities of TO and LO are asymmetric and the full width at half maximum (FWHM) of the LO peak is broadened from 4.2 to 9.3 cm^{-1}. The red shift, emergence of new features and broadened FWHM signify that the selection rules are perturbed enough for the reduction of grain size [24]. Quantitatively, an ~8 cm^{-1} red shift in frequency and a ~5 cm^{-1} augment in FWHM for LO modes correspond to crystallizes 5 to 6 nm in size [45], a 90% reduction compared with initial GaAs (~50 nm). Besides, after annealing [24], the LO frequency and FWHM of released GaAs are reversible which means the arsenic vacancies [45]. And, X-ray absorption also attests that it is partial amorphization [24]. Thus we can conclude that the lattice defects in released GaAs mainly include grain size reduction, arsenic vacancies, and partial amorphization.

According to the Raman analysis, we recognize that GaAs presents diverse structure transitions and vibrational properties at high pressure. To further explore their effect on κ and clarify the relationship between structure and performance, we performed high-pressure TDTR experiments.

3.2. Pressure-induced anomalous thermal conductivity of GaAs

Previous calculations on κ_{GaAs} [27] indicate that pressure induces the increase in phonon group velocity coupled with the decrease in relaxation time. These two factors' competing leads to the nonlinear increase in $\kappa_{ZB\text{-GaAs}}$. Regarding to *Cmcm* phase, the three-phonon processes are more easily so that the phonon relaxation time is much lower than that of the *ZB* phase, resulting in ultralow lattice thermal conductivity. Nevertheless, according to our Raman analysis, the GaAs undergoes multi-level transformations in experiments, such as the plastic deformation, *ZB* to *Cmcm* phase, hysteresis from *Cmcm* to *ZB*, reduction of grain size, arsenic va-

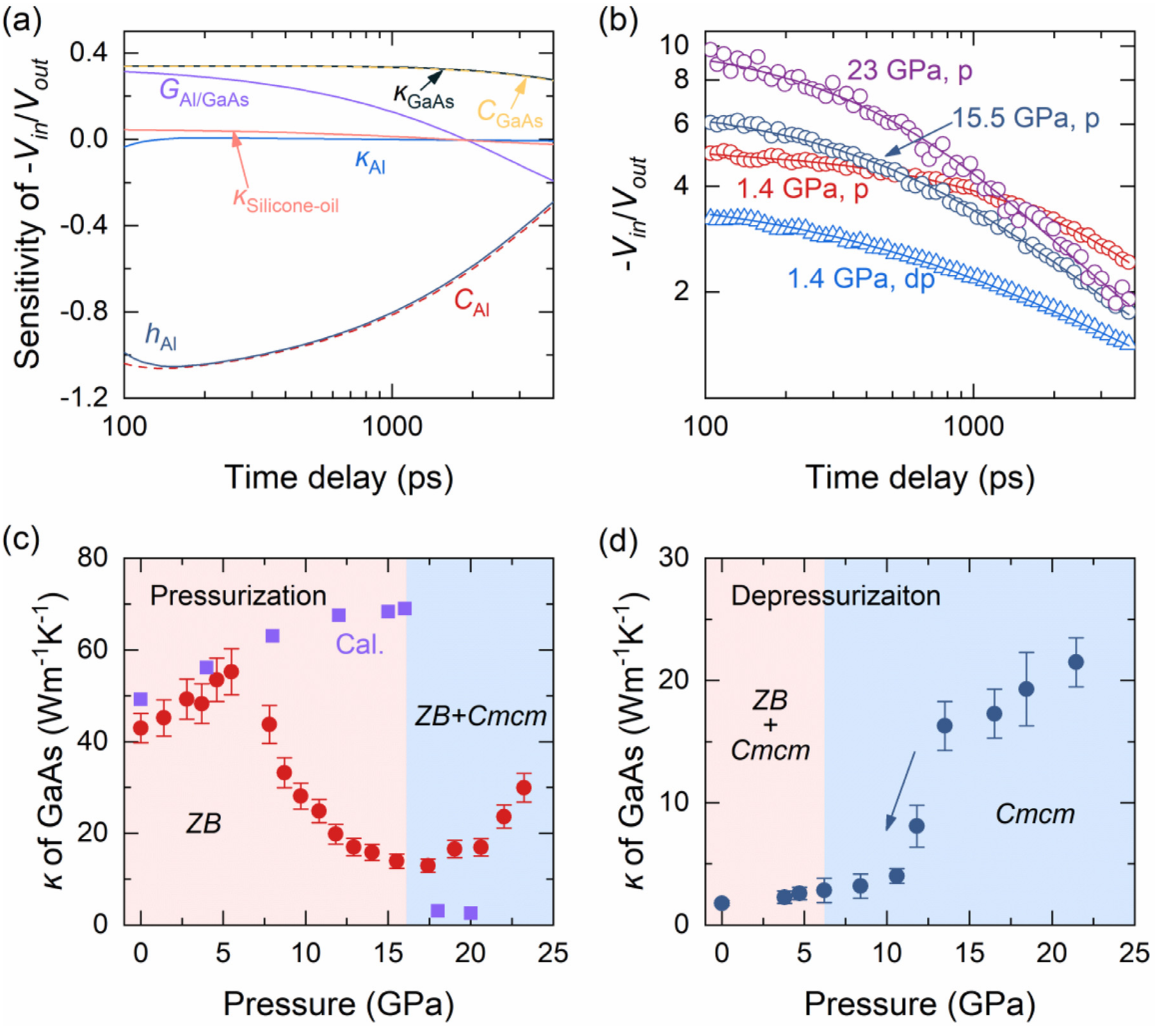

Fig. 4. Thermal conductivity of GaAs at high-pressure. (a) The sensitivity of key parameters to $-V_{\text{in}}/V_{\text{out}}$ signals at 1.4 GPa. κ, G, C, and h denote thermal conductivity, interfacial thermal conductance, volumetric heat capacity, and thickness, respectively. (b) The ratio signals at the selected pressure (circles for pressurization and triangles for depressurization) compared with the bidirectional heat transport model as a function of the delay time. The measured pressure-dependence in κ_{GaAs} during (c) pressurization and (d) depressurization processes. The calculated lattice κ_{GaAs} is taken from Ref. [24] (purple squares).

cancies, and partial amorphization. It is far beyond the power of theoretical calculations to study these complex transitions, and the experiment is necessary.

In the experiment, analyzing TDTR signals requires the adjustment of unknown parameters to minimize the differences between the experimental data and the heat transport model. Bidirectional heat flows into both samples and silicone oil are considered in the model [38]. Besides the κ_{GaAs} and $G_{\text{Al/GaAs}}$ are to be fitted, other parameters are determined carefully, including κ of silicone-oil and Al, volumetric heat capacity C of silicone-oil, Al, and GaAs (Fig. S1 in the Supplemental Material), and thickness h of Al (Fig. S2).

For the multi-parameters coupled case, sensitivity analysis [46] is a useful tool to directly observe the interaction between various parameters and examine whether interesting parameters can be measured with good accuracy. The sensitivity analysis is shown in Fig. 4(a) and we find that κ_{GaAs} and $G_{\text{Al/GaAs}}$ have high and separable sensitivities to TDTR signals and thus can be measured accurately and simultaneously. Fig. 4(b) illustrates the ratio signals at the selected pressure fitted with the bidirectional heat transport model as a function of delay time. The ratio signals have a sine-like oscillation within 300 ps owing to the Brillouin scattering of silicone oil, and the Brillouin frequency is 17 GHz at ~1.4 GPa and 37 GHz at ~23 GPa (Fig. S3), which matches well with the literature values [31]. It reflects that the silicone oil still surrounds the sample under such high pressure, avoiding the damage to the sample caused by direct contact with anvils.

The pressure-dependent κ_{GaAs} is shown in Fig. 4(c, d). In the pressurization process, the κ_{GaAs} shows a sine-like trend and can be divided into three stages. (i) The κ_{GaAs} has a positive correlation with pressure in the range of 0–6.4 GPa and the increment is about 28%. This stage consists of elastic deformation regions shown in Fig. S2(a). Our experimental results match well with the previous calculation results [27], which experimentally proves that phonon group velocity and relaxation time compete with each other, and the former plays a dominant role. (ii) Contrary to the results of the first-principles calculations, the κ_{GaAs} begins to decrease until ~16 GPa, where the phase transition from *ZB* to *Cmcm* occurs. The κ_{GaAs} is 13 ± 1.5 W m^{-1} K^{-1} at ~16 GPa, a 76% reduction from the highest value. This stage agrees well with the plastic deformation regions (Fig. S2(a)). The plastic deformation can induce the emergence of various lattice defects such as dislocations and twin crystals, which enhance lattice anharmonicity and strongly suppress the phonon relaxation time. Therefore, lattice defects play a central role in the decrease of κ_{GaAs} in this stage. (iii) With further increased pressure, the κ_{GaAs} rises monotonously again. We emphasize that for the pressure above ~16 GPa, the partial *ZB*-GaAs is converted into *Cmcm*-GaAs (metal phase), which is evidenced by the Raman analysis (Fig. 2(c)). For the two-phase coexistence case, two factors, lattice thermal conductivity κ_1 and electron thermal conductivity κ_e, contribute to the κ_{GaAs}. The κ_1 includes lattice thermal conductivity of *ZB*- and *Cmcm*-GaAs and κ_e is for *Cmcm*-GaAs. Similar to the second stage, the lattice defects continue to increase and the proportion of *ZB* phase is smaller and smaller, thus the κ_1 of *ZB* will decrease. Besides, prior calculations show that three-phonon processes are more easily, reducing κ_1 of *Cmcm*. Another factor is metallization, which allows free electrons to act as carriers for thermal transport. Recent work by Giri et al. [47] proposed that at high pressure, the reduction in the electron-phonon coupling factor leads to considerable increases in electron thermal conductivity. Therefore, the κ_e makes a dominant contribution to the increase of κ_{GaAs} in this stage.

热导率机理解释

Comparing experimental and theoretical results in the pressurization process, we can conclude that phonon group velocity and relaxation time compete with each other, making the nonlinear increase of κ_{GaAs} in elastic regions; lattice defects induced by plastic deformation dominate the decrease κ_{GaAs} in plastic regions; after the metallization, weakened electron-phonon coupling increases the κ_e in *Cmcm*-GaAs, which plays a dominant role in the increase of κ_{GaAs}.

Our Raman analysis suggests that GaAs is irreversible and there is a large hysteresis from *Cmcm* to *ZB*, however, these features cannot be captured by theoretical calculations. Therefore, we also measured the pressure-dependent κ_{GaAs} during the depressurization process, as presented in Fig. 4(d). We find that: (i) the κ_{GaAs} is reversible from 23 to 13.5 GPa, indicating that the structure is not further perturbed and that electrons still dominate the change in κ_{GaAs}. The Raman analysis also illustrates that there are indeed no phase transitions. (ii) When the pressure is lower than ~13.5 GPa, the κ_{GaAs} reduces dramatically. With the continued decompressing to ~6.4 GPa, the TO and LO modes reappear, indicating the transition from *Cmcm* to *ZB* phase with large hysteresis. The released GaAs shows a glass-like κ as 1.8 ± 0.2 W m^{-1} K^{-1}, a 96% reduction compared to the initial GaAs. Because it is still a metallic phase at ~13.5 GPa, we cannot directly obtain more structural information from the Raman signal except for that there is no phase transition or no new phase is created. Fortunately, we found that the released GaAs undergoes a reduction in grain size, arsenic vacancies, and partial amorphization by Raman spectrum. We also noticed that the $G_{\mathrm{Al/GaAs}}$ has an abrupt increase at such pressure for the amorphization of GaAs. Hence, we can infer that the abrupt decrease in κ_{GaAs} at ~13.5 GPa is mainly due to the onset of amorphization. Perhaps because of these defects, we do not observe that the *Cmcm* phase transforms to a Cinnabar phase [20] from the Raman scattering results. We also note that *Cmcm* to *ZB* phase hardly affects κ_{GaAs}, and therefore, grains reduction, arsenic vacancies, and partial amorphization are the major factors in the decreasing of κ_{GaAs}. Prior work has proved that the electrical conductivity of released GaAs has been improved by seven orders of magnitude [44], indicating that it is a promising candidate for thermoelectric materials. We also emphasize that since the GaAs is pure before dealing with it, it generates defects without introducing host atoms compared with the ways through electron or neutron bombardments, which will damage the mechanical strength [48].

3.3. *Pressure enhancing interfacial thermal conductance between Al and GaAs*

Utilizing pressure to modulate G also attracted great interest. As shown in Fig. 5(a), $G_{\mathrm{Al/GaAs}}$ is enhanced and gradually becomes saturated with compression, and similar behaviors are also found in previous works [13,31]. With pressure increased to ~23 GPa, $G_{\mathrm{Al/GaAs}}$ increases from 70 to 160 MW m^{-2} K^{-1}, a nearly 130% augment. During the depressurization (Fig. 5(b)), the $G_{\mathrm{Al/GaAs}}$ is considered to be reversible from ~23 to ~12 GPa, paralleling the behavior of κ_{GaAs}. Nevertheless, the G has a dramatic increase when the pressure is below 12 GPa. This phenomenon is also consistent with the pressure regions where κ_{GaAs} reduces dramatically (see Section 3.2). Therefore, it is natural to see that the lattice structure of GaAs has a synchronized effect on G and κ under high pressure. It is more complicated for revealing physical relationships between G and lattice structure, since G is not only a function of the materials comprising the interface (intrinsic), but also has a strong dependency on the atomic conditions around the interface (extrinsic).

The intrinsic part of G usually includes the transmission coefficient, group velocity, and PDOS. When thermal carriers are phonons, G is often assumed to be [49]:

$$G = \frac{1}{4}\sum_i \int t_\omega v_\omega \hbar\omega D_\omega \frac{\partial n_\omega}{\partial T} \mathrm{d}\omega_i, \tag{1}$$

where t_ω is the transmission coefficient, v_ω is the group velocity, D_ω is the density of states, and n_ω is the Bose-Einstein distribution function. The PDOS of crystalline Al (c-Al) and GaAs (c-GaAs) are from the first-principles calculations. As shown in Fig. 5(c), with the pressure increased, the PDOS of c-Al and c-GaAs is broadened and characteristic phonon frequencies shift towards higher frequencies, increasing the overlap of the PDOS as well as the number of phonons involved in interfacial thermal transport. Considering v_ω of both c-Al and c-GaAs also positively correlate with pressure [27,47], the intrinsic G should increase with pressure. On the other hand, the extrinsic part of G usually includes roughness, disorder, dislocations, and bonding conditions [30]. Note that the surface of GaAs usually has a natural oxide layer (~2 nm with low acoustic impedance), which acts as an acoustically soft layer between Al and GaAs. The bonding or stiffness of this "weak" interface will be enhanced with the pressurization, resulting in increasing G of the extrinsic part [29,50]. Therefore, from the above analysis, both intrinsic and extrinsic factors have positive contributions to the G from ambient to ~16 GPa, which is consistent with the experimental results. Besides, the measured $G_{\mathrm{Al/GaAs}}$ with some deviation after the metallization ($>$ 16 GPa) can be attributed to a more complex scattering of phonons, defects, and electrons across the interface [13].

During the depressurization, according to the Raman results and measured κ_{GaAs}, we believe the structure of GaAs is closer to amorphous while the pressure is lower than ~12 GPa. Here, we used the MD simulation to calculate the PDOS of amorphous GaAs (a-GaAs), and we also calculated the PDOS overlap factor which was defined as the integral of the overlap regions over the integral of the PDOS of c-Al. According to the PDOS overlap factor shown in Fig. 5(d), we find that the PDOS overlap between a-GaAs and c-Al is much larger than that between c-GaAs and c-Al, which means that Al phonons can participate much more in interfacial thermal transport across the Al/a-GaAs interface. In addition, from recent experimental [51] and theoretical [52] studies, it can be inferred that the diffusive vibrational modes across Al/a-GaAs interfaces may have a higher transmission coefficient than that of Al/c-GaAs interfaces [53]. Therefore, according to Eq. (1), we can conclude that the increased D_ω and t_ω make the $G_{\mathrm{Al/GaAs}}$ increase dramatically. Besides, the PDOS overlap at 0 and 10 GPa is almost the same and the transmission coefficient is considered pressure-independent [54]. When continuing depressurization to 0 GPa, the measured $G_{\mathrm{Al/GaAs}}$ gradually drops from 300 to 180 MW m^{-2} K^{-1}. Because the PDOS overlap factor has no obvious pressure

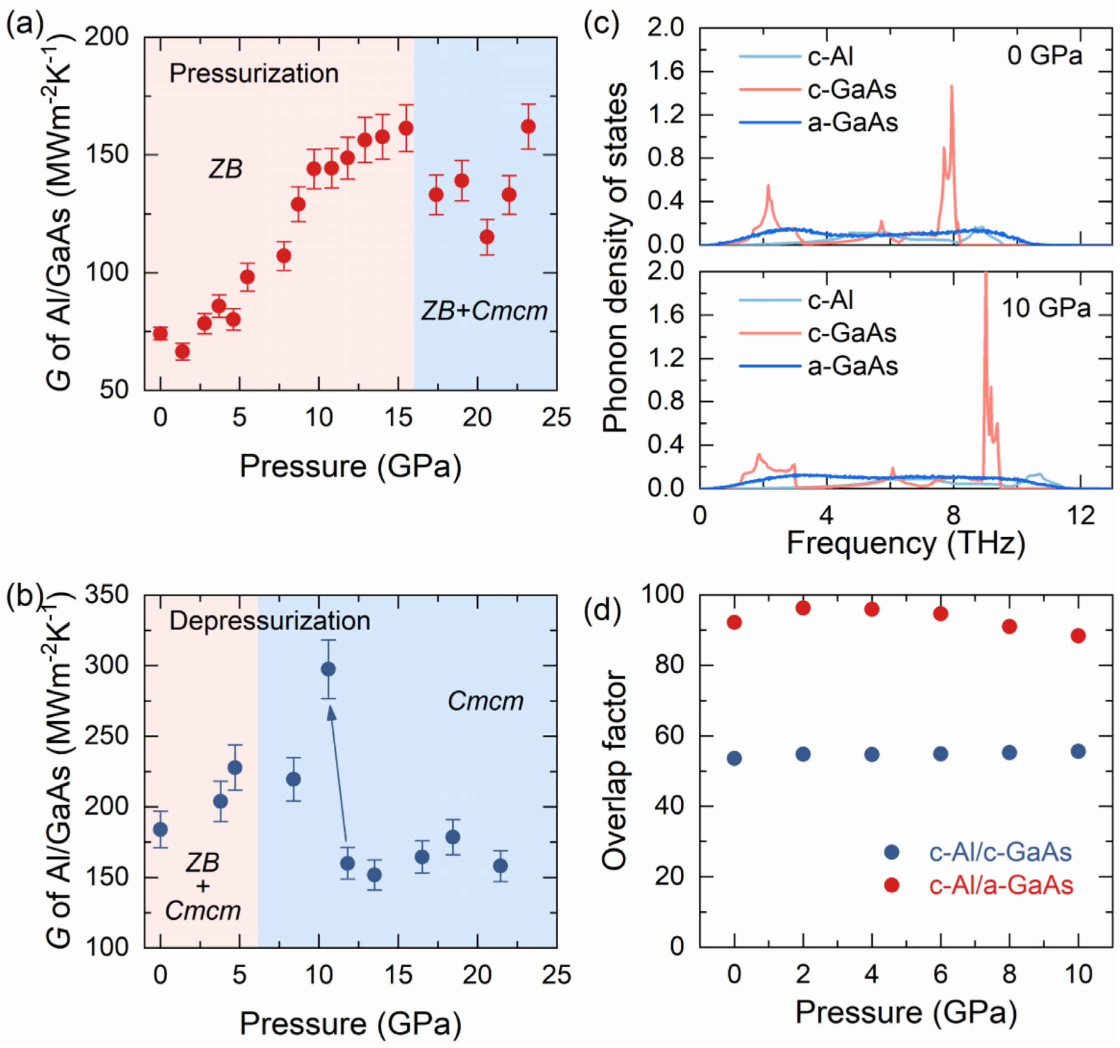

Fig. 5. Interfacial thermal conductance between Al and GaAs at high pressure The measured pressure-dependence in $G_{\mathrm{Al/GaAs}}$ during (a) pressurization and (b) depressurization processes. (c) PDOS of GaAs and Al at 0 and 10 GPa. a and c represent amorphous and crystalline, respectively. Crystalline PDOS is calculated by the first principles and amorphous PDOS is calculated by MD simulation. The PDOS of other pressure is shown in Fig. S4. (d) PDOS overlap factor of c-Al/c-GaAs and c-Al/a-GaAs as a function of pressure.

dependence, it can be attributed to the reduction of group velocity and interfacial stiffness. As the pressure is completely released, the $G_{\mathrm{Al/GaAs}}$ has not recovered to the initial value, but remains 2.6 times higher.

3.4. Correlations among lattice structure, thermal conductivity and interfacial thermal conductance in pressure cycles

During the pressure cycle, the lattice structure of GaAs undergoes diverse transitions, which is tracked by the Raman scattering and morphology evolution. Further experimental measurements and theoretical calculations on κ and G confirmed that thermal transport properties under high pressure are closely related to these structural transitions and can support each other. To make the structure-performance relationship clearer, we present all structure transitions and corresponding dominant factors shown in Fig. 6.

In the pressurization process, pressure-induced increase in GaAs phonon group velocity and decrease in relaxation time makes κ_{GaAs} increase monotonously in structural elastic deformation regions (0–6 GPa); dislocation and twin crystals induced by plastic deformation reduce the κ_{GaAs} greatly in 6–16 GPa; after metallization, the electron in *Cmcm*-GaAs dominates the re-increasing of κ_{GaAs}. Besides, the increase in intrinsic (PDOS overlap and group velocity) and extrinsic (interfacial bonding strength) factors have positive contributions to the $G_{\mathrm{Al/GaAs}}$ with pressure increase.

For the depressurization process, the κ_{GaAs} is reversible from 23 to 13.5 GPa and electrons remain the dominant factor. $G_{\mathrm{Al/GaAs}}$ has a parallel behavior with κ_{GaAs} in this pressure region. With continuing decompression, there is a significant reduction in κ_{GaAs} but a dramatic increment in $G_{\mathrm{Al/GaAs}}$. The lattice defects include grain size reduction, arsenic vacancies, and partial amorphization reduce the κ_{GaAs} and make released GaAs exhibit glass-like κ. The dramatic increase in $G_{\mathrm{Al/GaAs}}$ is due to the larger PDOS overlap and transmission coefficient between a-GaAs and c-Al. Besides, group velocity dominates the reduction in $G_{\mathrm{Al/GaAs}}$ from 300 to 180 MW m^{-2} K^{-1} with decompressing to ambient. As the pressure is completely released, $G_{\mathrm{Al/GaAs}}$ is 2.6 times higher than that of the initial.

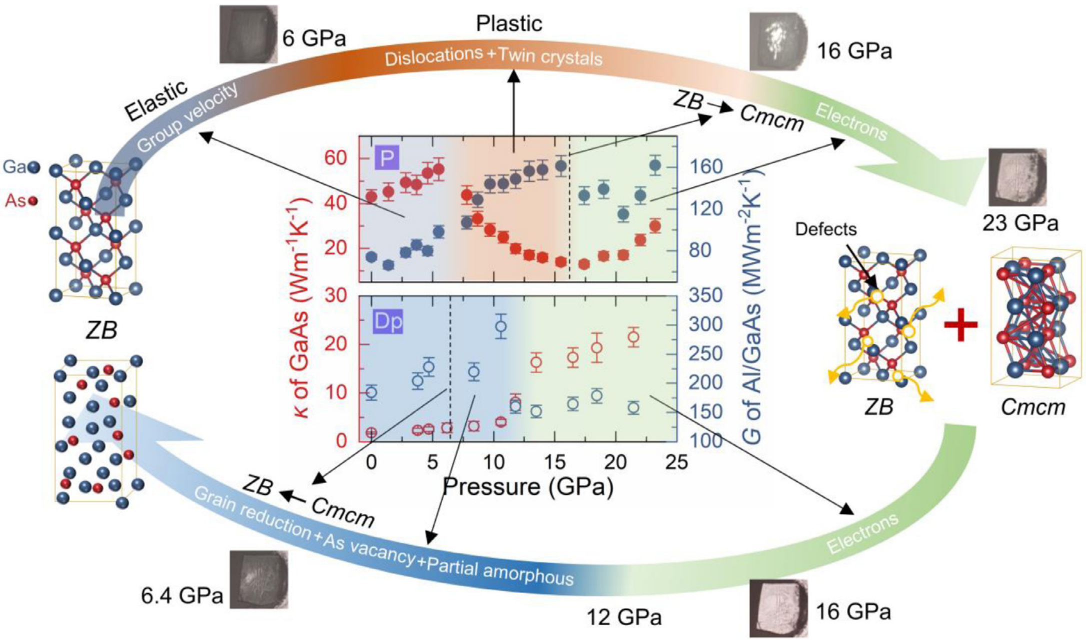

Fig. 6. The schematic diagram of all structure transitions in GaAs and its relationship with thermal transport properties in the pressure cycle.

4. Conclusions

In summary, we systematically investigated the κ_{GaAs} and $G_{\mathrm{Al/GaAs}}$ of all possible GaAs structures in pressure cycles using TDTR coupled with the DAC and Raman spectroscopy. During the pressurization process, phonon group velocity, lattice defects (dislocations and twin crystals), and electrons play a central role in κ_{GaAs} in elastic, plastic, and metallization regions, respectively. The increased PDOS overlap, group velocity, and interfacial bonding strength enhance $G_{\mathrm{Al/GaAs}}$. In the depressurization process, both κ_{GaAs} and $G_{\mathrm{Al/GaAs}}$ are reversible from 23 to 13.5 GPa. Electrons remain the dominant factor on κ_{GaAs}. $G_{\mathrm{Al/GaAs}}$ increase dramatically at ~12 GPa due to the larger PDOS overlap and transmission coefficient. With decompressing to ambient, lattice defects including grain size reduction, arsenic vacancies, and partial amorphization reduce the κ_{GaAs} and make the released GaAs exhibit glass-like κ. Besides, the group velocity is responsible for the reduction in $G_{\mathrm{Al/GaAs}}$. The completely released $G_{\mathrm{Al/GaAs}}$ is 2.6 times higher than that of the initial. Thus our findings open a new dimension in synergistically realizing glass-like thermal conductivity and enhancing interfacial thermal conductance, which can facilitate thermoelectric performance and its potential engineering applications.

Declaration of Competing Interest

The authors declare that they have no known competing financial interests or personal relationships that could have appeared to influence the work reported in this paper

Acknowledgments

This work was financially supported by the National Natural Science Foundation of China (Nos. 51720105007, 51976025, and 52206219) and the Fundamental Research Funds for the Central Universities (No. DUT22ZD216).

Supplementary materials

Supplementary material associated with this article can be found, in the online version, at doi:10.1016/j.jmst.2022.10.009.

References

[1] X. Dong, A.R. Oganov, A.F. Goncharov, E. Stavrou, S. Lobanov, G. Saleh, G.R. Qian, Q. Zhu, C. Gatti, V.L. Deringer, R. Dronskowski, X.F. Zhou, V.B. Prakapenka, Z. Konôpková, I.A. Popov, A.I. Boldyrev, H.T. Wang, Nat. Chem. 9 (2017) 440–445.
[2] J. Lin, H. Chen, Y. Gao, Y. Cai, J.B. Jin, A.S. Etman, J. Kang, T. Lei, Z.N. Lin, M.C. Folgueras, L.N. Quan, Q. Kong, M. Sherburne, M. Asta, J.L. Sun, M.F. Toney, J.Q. Wu, P.D. Yang, Proc. Natl. Acad. Sci. U. S. A. 116 (2019) 23404.
[3] E. Burzo, P. Vlaic, D.P. Kozlenko, N.O. Golosova, S.E. Kichanov, B.N. Savenko, A. Ostlin, L. Chioncel, J. Mater. Sci. Technol. 42 (2020) 106–112.
[4] S. Raymond, J. Bouchet, G.H. Lander, M. Le Tacon, G. Garbarino, M. Hoesch, J.P. Rueff, M. Krisch, J.C. Lashley, R.K. Schulze, R.C. Albers, Phys. Rev. Lett. 107 (2011) 136401.
[5] H. Yu, L.C. Chen, H.J. Pang, X.Y. Qin, P.F. Qiu, X. Shi, L.D. Chen, X.J. Chen, Mater. Today Phys. 5 (2018) 1–6.
[6] W.P. Hsieh, A.F. Goncharov, S. Labrosse, N. Holtgrewe, S.S. Lobanov, I. Chuvashova, F. Deschamps, J.F. Lin, Nat. Commun. 11 (2020) 3332.
[7] H. Zhou, D.K. Wang, Z. Li, J.Z. Cong, Z.Y. Yu, S. Zhao, P. Jiang, D.Y. Cong, X.Q. Zheng, K.M. Qiao, H. Zhang, J. Mater. Sci. Technol. 114 (2022) 73–80.
[8] C. Hernandez, S.K. Gupta, J.P. Zuniga, J. Vidal, R. Galvan, H. Guzman, L. Chavez, K. Lozano, Y. Mao, J. Mater. Sci. Technol. 66 (2021) 103–111.
[9] S. Stackhouse, L. Stixrude, B.B. Karki, Phys. Rev. Lett. 104 (2010) 208501.
[10] Y. Sun, J. Lv, Y. Xie, H.Y. Liu, Y.M. Ma, Phys. Rev. Lett. 123 (2019) 097001.
[11] W.P. Hsieh, M.D. Losego, P.V. Braun, S. Shenogin, P. Keblinski, D.G. Cahill, Phys. Rev. B 83 (2011) 174205.
[12] G.M. Manthilake, N. de Koker, D.J. Frost, C.A. McCammon, Proc. Natl. Acad. Sci. U. S. A. 108 (2011) 17901.
[13] G.T. Hohensee, M.R. Fellinger, D.R. Trinkle, D.G. Cahill, Phys. Rev. B 91 (2015) 205104.
[14] X.H. Meng, T. Pandey, J. Jeong, S.Y. Fu, J. Yang, K. Chen, A. Singh, F. He, X.C. Xu, J.S. Zhou, W.P. Hsieh, A.K. Singh, J.F. Lin, Y.G. Wang, Phys. Rev. Lett. 122 (2019) 155901.
[15] H.J. Joyce, Q. Gao, J. Wong-Leung, Y. Kim, H.H. Tan, C. Jagadish, IEEE J. Sel. Top. Quantum Electron. 17 (2011) 766–778.
[16] X.Q. Li, S.S. Lin, X. Lin, Z.J. Xu, P. Wang, S.J. Zhang, H.K. Zhong, W.L. Xu, Z.Q. Wu, W. Fang, Opt. Express 24 (2016) 134–145.
[17] S.B. Zhang, M.L. Cohen, Phys. Rev. B 35 (1987) 7604–7610.
[18] J. Crain, R.O. Piltz, G.J. Ackland, S.J. Clark, M.C. Payne, V. Milman, J.S. Lin, P.D. Hatton, Y.H. Nam, Phys. Rev. B 50 (1994) 8389–8401.
[19] M.I. McMahon, R.J. Nelmes, Phys. Status Solidi B-Basic Res. 198 (1996) 389–402.
[20] M.I. McMahon, R.J. Nelmes, Phys. Rev. Lett. 78 (1997) 3697–3700.
[21] A. Mujica, A. Muñoz, R.J. Needs, Phys. Rev. B 57 (1998) 1344–1347.
[22] M.I. McMahon, R.J. Nelmes, D.R. Allan, S.A. Belmonte, T. Bovornratanaraks, Phys. Rev. Lett. 80 (1998) 5564–5567.
[23] M.I. McMahon, R.J. Nelmes, Phys. Rev. Lett. 95 (2005) 215505.
[24] J.M. Besson, J.P. Itié, A. Polian, G. Weill, J.L. Mansot, J. Gonzalez, Phys. Rev. B 44 (1991) 4214–4234.
[25] A.M. Hofmeister, Proc. Natl. Acad. Sci. U. S. A. 104 (2007) 9192.

[26] R. Muthaiah, J. Garg, Phys. Chem. Chem. Phys. 22 (2020) 20914–20921.
[27] Z.H. Sun, K.P. Yuan, X.L. Zhang, D.W. Tang, Phys. Chem. Chem. Phys. 20 (2018) 30331–30339.
[28] W.P. Hsieh, B. Chen, J. Li, P. Keblinski, D.G. Cahill, Phys. Rev. B 80 (2009) 180302.
[29] W.P. Hsieh, A.S. Lyons, E. Pop, P. Keblinski, D.G. Cahill, Phys. Rev. B 84 (2011) 184107.
[30] R.B. Wilson, B.A. Apgar, W.P. Hsieh, L.W. Martin, D.G. Cahill, Phys. Rev. B 91 (2015) 115414.
[31] G.T. Hohensee, R.B. Wilson, D.G. Cahill, Nat. Commun. 6 (2015) 6578.
[32] G.T. Hohensee, W.P. Hsieh, M.D. Losego, D.G. Cahill, Rev. Sci. Instrum. 83 (2012) 114902.
[33] H.K. Mao, X.J. Chen, Y. Ding, B. Li, L. Wang, Rev. Mod. Phys. 90 (2018) 015007.
[34] D.G. Cahill, Rev. Sci. Instrum. 75 (2004) 5119–5122.
[35] J. Zhu, X.W. Wu, D.M. Lattery, W. Zheng, X.J. Wang, Nanoscale Microscale Thermophys. Eng. 21 (2017) 177–198.
[36] P.Q. Jiang, X. Qian, R.G. Yang, J. Appl. Phys. 124 (2018) 161103.
[37] K. Kang, Y.K. Koh, C. Chiritescu, X. Zheng, D.G. Cahill, Rev. Sci. Instrum. 79 (2008) 114901.
[38] A. Schmidt, M. Chiesa, X.Y. Chen, G. Chen, Rev. Sci. Instrum. 79 (2008) 064902.
[39] P. Giannozzi, S. Baroni, N. Bonini, M. Calandra, R. Car, C. Cavazzoni, D. Ceresoli, G.L. Chiarotti, M. Cococcioni, I. Dabo, A. Dal Corso, S. de Gironcoli, S. Fabris, G. Fratesi, R. Gebauer, U. Gerstmann, C. Gougoussis, A. Kokalj, M. Lazzeri, L. Martin-Samos, N. Marzari, F. Mauri, R. Mazzarello, S. Paolini, A. Pasquarello, L. Paulatto, C. Sbraccia, S. Scandolo, G. Sclauzero, A.P. Seitsonen, A. Smogunov, P. Umari, R.M. Wentzcovitch, J. Phys. Condes. Matter. 21 (2009) 395502.
[40] M. Schlipf, F. Gygi, Comput. Phys. Commun. 196 (2015) 36–44.
[41] S. Plimpton, J. Comput. Phys. 117 (1995) 1–19.
[42] D.A. Murdick, X.W. Zhou, H.N.G. Wadley, D. Nguyen-Manh, R. Drautz, D.G. Pettifor, Phys. Rev. B 73 (2006) 045206.
[43] D.T. Morelli, V. Jovovic, J.P. Heremans, Phys. Rev. Lett. 101 (2008) 035901.
[44] J. Wang, B.J. Wu, G.Z. Zhang, L.H. Tian, G.R. Gu, C.X. Gao, RSC Adv. 6 (2016) 10144–10149.
[45] R.S. Berg, P.Y. Yu, Phys. Rev. B 35 (1987) 2205–2221.
[46] D.M. Hamby, Environ. Monit. Assess. 32 (1994) 135–154.
[47] A. Giri, J.T. Gaskins, L. Li, Y.S. Wang, O.V. Prezhdo, P.E. Hopkins, Phys. Rev. B 99 (2019) 165139.
[48] Z.W. Duan, X.Y. Zhao, J. Xu, P. Wang, W.M. Liu, Appl. Surf. Sci. 480 (2019) 438–447.
[49] R.J. Stoner, H.J. Maris, Phys. Rev. B 48 (1993) 16373–16387.
[50] L. Zhang, P. Keblinski, J.S. Wang, B. Li, Phys. Rev. B 83 (2011) 064303.
[51] J. Kimling, A. Philippi-Kobs, J. Jacobsohn, H.P. Oepen, D.G. Cahill, Phys. Rev. B 95 (2017) 184305.
[52] K. Gordiz, M.G. Muraleedharan, A. Henry, J. Appl. Phys. 125 (2019) 135102.
[53] A. Giri, J.L. Braun, P.E. Hopkins, J. Appl. Phys. 119 (2016) 235305.
[54] M. Shen, W.J. Evans, D. Cahill, P. Keblinski, Phys. Rev. B 84 (2011) 195432.